ELSEVIER

Contents lists available at ScienceDirect

Geoenergy Science and Engineering

journal homepage: www.sciencedirect.com/journal/geoenergy-science-and-engineering



Upscaling reactive transport models from pore-scale to continuum-scale using deep learning method

Jiahui You, Kyung Jae Lee

Department of Petroleum Engineering, University of Houston, Houston, USA

ARTICLE INFO

Keywords: Reactive transport Acid dissolution Upscaling method Pore-scale modeling Continuum-scale modeling Convolutional neural networks

ABSTRACT

Reactive transport modeling of subsurface environments plays an important role in addressing critical problems of geochemical processes, such as dissolution and precipitation of minerals. Current transport models for porous media span various scales, ranging from pore-scale to continuum-scale. In this study, we established an upscaling method connecting pore-scale and continuum-scale models by employing a deep learning methodology of Convolutional Neural Networks (CNNs). We applied Darcy-Brinkmann-Stokes (DBS) method to simulate the fluid flow and reactive transport in pore-scale models, which would act as constituents of a continuum-scale model. The datasets of spatial pore distribution of subvolume samples were used as the input for the deep learning model, and the continuum (Darcy)-scale parameters such as permeability, effective surface area, and effective diffusion coefficient were figured out as outputs (i.e., labels). By applying the trained models of the subvolumes in the entire sample volume, we generated the initial field of porosity, permeability, effective diffusion coefficient, and effective surface area for continuum-scale simulation of a mineral dissolution problem. We took an acid dissolution case as an example to utilize the outcomes of trained deep learning models as input data in the continuum-scale simulation. This work presents a comprehensive upscaling workflow, as bridging the findings of microscale simulations to the continuum-scale simulations of a reactive transport problem.

1. Introduction

Reactive transport modeling of subsurface systems can help address various geochemical processes, such as dissolution and precipitation of minerals. However, characteristics of subsurface porous media, such as high heterogeneity and intricate and irregular structures, it's challenging to efficiently and reliably compute the solutions of complex problems where reactive transport occurs. In addition, transport models of porous media are in different scales spanning from pore-scale to continuum-scale and require reliable upscaling techniques to establish the connection between these models.

Diverse numerical methods have been proposed to address reactive transport in various scales, including pore network model, capillary tube model, continuum (Darcy)-scale model, and pore-scale models (Algive et al., 2009; Dormieux and Lemarchand, 2001; Estermann and Scheiner, 2018; Hung et al., 1989; Lichtner and Kang, 2007; Liu et al., 2013; Maheshwari et al., 2013, 2016; Panga et al., 2005; Pivonka et al., 2004; Ratnakar et al., 2013). In continuum-scale models, porous media is described with continuous and utilizes averaged properties at a

macroscopic scale. In contrast, pore-scale models aim to capture the intricate details of fluid transport processes occurring at the microscale level, as separately describing pore zones and minerals. Thus, continuum-scale models can be used to capture the long-term behavior of fluid in large scale, while pore-scale models can provide the insights of fluid-rock interaction in heterogeneous and complex structures of pores. There are various numerical discretization methods, which can be applied for reactive transport problems, such as Lattice Boltzmann Method (LBM), Finite Volume Method (FVM), and Integral Finite Difference (IFD) method. In LBM, fluid is represented by a set of distribution functions defined on a lattice. The distribution functions propagate and collide at each lattice point, as simulating the movement and interaction of fluid particles. TOUGHREACT, a multiphase reactive transport code based on TOUGH2, employs IFD method to solve governing equations of fluid and heat flow and chemical transport in sequence, which enables the flexible discretization of macroscale models of geologic media (Xu et al., 2004). In the FVM, terms in the conservation equation are turned into face fluxes and evaluated at the finite volume faces, as guaranteeing the strict mass conservation in the system

E-mail address: kjlee6@central.uh.edu (K.J. Lee).

^{*} Corresponding author.

(Moukalled et al., 2016). Where, unknow variables are saved in the centroid of volume element, which enables the implementation of various boundary conditions. Thus, FVM method provides a robust and versatile framework for describing complex physical processes in various applications (You and Lee, 2021b). Oliveira used FVM method to solve the Navier-Stokes equations and the advection-diffusion equation to obtain species' concentration in the pore-scale model (Oliveira et al., 2019). In another study, a combined FVM and LBM method was employed to solve the reactive transport in the system with multi-minerals and rock heterogeneity (Liu et al., 2017). In their work, LBM method and FVM method were used to discretize governing equations for fluid flow and species' concentration, respectively. Darcy-Brinkmann-Stokes (DBS)-employed FVM enables the microscale investigation of complex phenomena in subsurface porous media, and it has been applied to various problems of reactive transport modeling (Minto et al., 2019; Molins et al., 2020). Soulaine and Tchelepi (2016) applied the DBS method to various subsurface processes, including fluid flow in fractured porous media, mineral dissolution, and shale pyrolysis (Soulaine and Tchelepi, 2016). Liu and Mostaghimi (2018) applied the DBS method to describe carbonate dissolution (Liu and Mostaghimi, 2018). In their later work, they considered the movement of detached particles during the dissolution, which provided an insight into particle clogging in the dissolved fractures (Liu et al., 2020). DBS-employed FVM models can be benefited from the direct use of digital rock images of porous media as the computational domains in pore-scale models, but one of its difficulties is the demanding memory and time for computations, especially when high-resolution 3-D images are used. For example, model geometries based on X-ray tomograms are often consisted of a huge number of voxels ($>10^9$) and hence requires massive computational cost (Prasianakis et al., 2020).

Given the above-mentioned difficulties and the multiscale nature of porous media, researchers have actively explored the application of advanced AI techniques such as Convolutional Neural Networks (CNNs), to resolve the challenges of reactive transport modeling problems in porous media (Alqahtani et al., 2020; Prasianakis et al., 2020; Röding et al., 2020; Wu et al., 2019). Wu et al. predicted the effective diffusion coefficient of porous media with 2D digital rock images, by applying the LBM method and CNNs modeling capability (Wu et al., 2019). Where, the CNNs model provided better prediction of effective diffusion coefficient than the empirical Bruggeman equation, especially for the porous media with low diffusivity. In another study, the microstructures of 2D images of porous media were generated using the quartet structure generation set (OSGS) method (Wang et al., 2007). In their study, the relationship between fluid permeabilities and a variety of microstructural descriptors was reported. Their training data included a set of 30, 000 virtual 3-D porous microstructures of various types (Röding et al., 2020). These studies were based on artificially synthesized pore-scale geometric models. On the other hand, several studies investigated the application of deep learning technologies on the real digital rock images obtained with X-ray or X-ray Computed Tomography (CT) for reactive transport problems. Prasianakis et al. trained a shallow neural network based on the results of microscopic geochemical reactive transport simulations, and integrated it into a continuum-scale reactive transport modeling code (Prasianakis et al., 2020). Their study suggested that the neural-network-coupled simulation performed better than the full speciation reactive transport simulations, both in terms of computational efficiency and memory usage. Alqahtani et al. trained the CNNs model by taking micro-CT images as input and computed outputs by numerical simulations (Algahtani et al., 2020). Their trained model could be used to predict the physical properties of porous media, such as porosity, specific surface area, and average pore size, where, the datasets were created from sub-divided tomograms of three different sandstones. The datasets were consisted of 5262 training images and 2000 test images.

Besides CNNs, some researchers used other machine learning algorithms to investigate the characteristics of porous media. In one study of

pore-scale reactive transport modeling, effective reaction rates were calculated based on the distribution profiles of reactant concentration (Liu et al., 2022). Where, pore structural features such as specific surface area, pore sphericity, and coordination number were extracted from pore-scale modeling. They first used the Random Forest (RF) learning model to rank the importance of features and used the first three most important features to train an Artificial Neural Network (ANN) model and accurately predicted the effective reaction rates. In another study of Menke et al., they divided Estaillages limestone into 60³ and 120³ subvolumes of voxels and calculated permeability on these subvolumes using DBS method (Menke et al., 2021). The extracted features such as porosity, cumulative phase connectivity, and phase volume fraction were taken as input data, and the calculated permeability from DBS method was taken as output data. They showed the 80 times less computational expense through the application of machine learinig technologies.

Heterogeneous and irregular structures of porous media present significant challenges for direct simulation, as hindering the formulation of universal relationships and equations to accurately describe the fluid flow and reactive transport characteristics within them. Conducting simulations on high-resolution digital rock images can be both costly and time-consuming, as posing challenges when attempting to upscale these pore-scale parameters to a larger scale model. Consequently, accurate estimation of the intrinsic properties of porous media becomes difficult, leading to higher uncertainties in the upscaling processes. As abovementioned, however, recent advancements in machine learning techniques enable the prediction of these crucial properties without the need for time-consuming simulations (Tahmasebi et al., 2020). While the training process of machine learning methods can demand a significant amount of time, they can quickly estimate the properties of interest for new samples within multiple seconds, once the training process is completed.

In this study, we apply the DBS method to simulate the fluid flow and reactive transport process in pore-scale models, which are to act as constituents of a continuum-scale model. The obtained results are to be used to train the CNNs deep leaning models. The input features are consisted of the spatial distribution and structure of micropores, while the outputs for the deep learning models include the permeability, effective surface area, and effective diffusion coefficient of subvolume. Here, we divide one of the high resolution 3-D digital rock images into 4096 subvolumes, where each subvolume had a resolution of 50 \times 50 \times 50 voxels, and apply the trained models to obtain the outputs, which are initialized as input parameters for continuum-scale reactive transport modeling. The workflow of this study presents the robust upscaling process, as connecting the insights obtained from pore-scale modeling to the input parameters of continuum-scale modeling. This paper is organized as follows: Section 2 introduces the mathematical formulations of pore-scale and continuum-scale models and the structure of deep learning neural network with CNNs. Sections 3 presents the results and discussion, and Section 4 presents the conclusion, respectively.

2. Methodology

2.1. Pore-scale modeling employing DBS method

In a Darcy-brinkman-Stokes (DBS) model, the whole computational domain is discretized into orthometric cells (Soulaine et al., 2017). Local porosity (ε) represents the volume fraction of either pore zone or solid zone within a pore-scale model. In the fluid area, $\varepsilon_f=1$ and $\varepsilon_s=0$; in the solid zone, $\varepsilon_f=0$ and $\varepsilon_s=1$; in the solid-liquid interface, $0<\varepsilon_f<1$; as such, each zone satisfies the relationship of $\varepsilon_s+\varepsilon_f=1$. In the DBS method, Darcy's law describes the fluid flow at the interface of solid and liquid, while the Navier-Stokes equation describes the fluid flow in pores. The governing equations are as follows (Soulaine et al., 2017; Soulaine and Tchelepi, 2016; You and Lee, 2021a, 2021c).

$$\frac{1}{\varepsilon_f} \left(\frac{\partial \rho_f \overline{v}_f}{\partial t} + \nabla \bullet \left(\frac{\rho_f}{\varepsilon_f} \overline{v}_f \overline{v}_f \right) \right) = -\nabla \overline{\rho}_f + \frac{\mu_f}{\varepsilon_f} \nabla^2 \overline{v}_f - \mu_f k^{-1} \overline{v}_f$$
 (1)

$$k^{-1} = k_0^{-1} \frac{\left(1 - \varepsilon_f\right)^2}{\varepsilon_f^3} \tag{2}$$

where, \bar{v}_f is the average velocity; \bar{p}_f is the average pressure; μ_f is the dynamic viscosity; ρ_f is the fluid density in the system. The last term $(\mu_f k^{-1} \bar{v}_f)$ is the Darcy resistance term by the momentum exchange between fluid and solid phases (Soulaine et al., 2017). k is the local permeability, which is computed by the Kozeny-Carman relationship, $k^{-1} = k_0^{-1} \frac{(1-\epsilon_f)^2}{\epsilon_f^3}$. Where, k_0 is the initial local permeability, which is assumed to be 10^{-15} m² in this study. The advection–diffusion equation and mass conservation equation are as follows.

$$\frac{\partial \varepsilon_f \rho_f \overline{\omega}_{f,A}}{\partial t} + \nabla \bullet \left(\rho_f \overline{v}_f \overline{\omega}_{f,A} \right) = \nabla \bullet \left(\varepsilon_f \rho_f D_A^* \nabla \overline{\omega}_{f,A} \right) - \dot{m}_A \tag{3}$$

$$\dot{m}_A = \rho_f a_v r \overline{\omega}_{fA} \tag{4}$$

where, $\overline{w}_{f,A}$ is the concentration of species; in the application in this study of acid dissolution, subscript A indicates acid. D_A^* is the effective diffusion coefficient of acid; \dot{m}_A is the mass change rate of acid by mineral dissolution; r is the reaction rate of mineral dissolution; a_v is the effective surface area, which is calculated by $a_v = \|\nabla \varepsilon_f\| 4\varepsilon_f (1 - \varepsilon_f)$. We take volumetric average to quantify the effective surface area of the whole subvolume. $\langle a_v \rangle$ denotes the volumetric average of the effective surface area, which is computed as follows.

$$\langle a_v \rangle = \frac{1}{\Delta V} \int_{\Delta V} a_v dV \tag{5}$$

where, ΔV is the control volume.

Average permeability of a whole pore-scale model (i.e., constituent of continuum-scale model), K, is computed by the following equation adapted from the Darcy's Law.

$$K = -\frac{\langle \overline{v}_f \rangle \mu_f}{\langle \nabla \overline{p}_f \rangle} \tag{6}$$

where, the volumetric average velocity of fluid and pressure are calculated from the pore-scale simulation by $\langle \overline{\nu}_f \rangle = \frac{1}{\Delta V} \int_{\Delta V} \overline{\nu}_f dV$ and $\langle \overline{p}_f \rangle = \frac{1}{\Delta V} \int_{\Delta V_f} \overline{p}_f dV$, respectively. Here, ΔV denotes the fluid volume in the pore-scale model.

Based on the abovementioned governing equations, pore–scale reactive transport model was developed based on OpenFOAM, an open–source Computational Fluid Dynamics (CFD) platform (Weller et al., 1998). The governing equations were discretized by the FVM method. The initial and boundary conditions were set as follows: $\overline{v}_f|_{t=0} = \overline{v}_{f0}, \ \overline{v}_f|_{x=0} = \overline{v}_{f0}, \ \overline{v}_{f|_{x=0}} = 0, \ \overline{p}_f|_{x=x0} = \overline{p}_{out}, \ \omega_{f,i}|_{x=0} = \omega_{f,i0}, \ \text{and} \ \omega_{f,i}|_{t=0} = 0.$

2.2. Architecture of deep learning model

2.2.1. Convolutional Neural Networks (CNNs)

In ANN architecture, each neuron in one layer is connected to every neuron in the subsequent layer. This fully connected structure leads to a large number of connections, making it computationally expensive, especially when handling the high-dimensional data such as digital rock images. In contrast, neurons in CNNs architecture are arranged in a grid-like structure, representing the spatial dimensions of the input data. Thus, CNNs preserves the spatial relationship between inputs and feature maps, and enables the weight reusing which allows the network to detect and learn similar features or patterns at different spatial locations (Alqahtani et al., 2020). Thus, CNNs can take advantage of

effectively capturing local patterns and spatial correlations with the reduced number of learning parameters, while improving the ability to learn different patterns. Traditionally, CNNs have been used to recognize image-driven patterns or dataset by employing high-dimensional organization of neurons (Albawi et al., 2017).

2.2.2. Fully connected layer and convolutional layer

In a fully connected layer, each neuron in current layer is connected to every neuron in the subsequent layer. A fully connected layer is a fundamental building block of a Multi-Layer Perceptron (MLP) (Murtagh, 1991). It consists of an input layer, hidden layer, and output layer. The fully connected layer structure is described in the following equations (Zhang et al., 2021). Here, \boldsymbol{X} represents input matrix; \boldsymbol{H} represents the hidden layer; and \boldsymbol{O} represents the output layer. \boldsymbol{W} and \boldsymbol{b} denote weight vector and bias vector, respectively.

$$H = XW^{(1)} + b^{(1)} \tag{7}$$

$$O = XW^{(2)} + b^{(2)}$$
 (8)

where, superscripts represent the weights and biases at different layers. Activation functions introduce non-linear transformations to the weighted sum of inputs, allowing the neural network to learn complex relationships between the input and output. Activation function is applied to the output of each neuron in the output layer. The most commonly used activation function is Rectified Linear Unit (ReLU), Sigmoid, and Hyperbolic Tangent (tanh) (Sharma et al., 2017). Among them, ReLU($f(x) = \max(0, x)$) stands out due to its advantages in calculation efficiency and ability to mitigate the vanishing and exploding gradient problems (Sharma et al., 2017). This is because, ReLU function introduces non-linearity and prevents gradients from becoming significantly small during the backpropagation. The outputs of ReLU are all positive values, which can decrease gradient exploding. Instead of exponential operation, which has high cost on GPU calculation, ReLU function sets all negative values to zero and keeps positive values unchanged, making it highly efficient for the implementation on Graphics Processing Units (GPUs).

In this study, the spatial distributions of pores and grains are described in a set of 3-D data with width, height, and depth. If fully connected layers are applied to each grid, computational load gets enormously large. Thus, instead of applying full-size weights and biases, CNNs defines the kernel matrix with dimensions of a \times b \times c, and applies kernel across the entire input space. Thus, the 3-D convolutional layer can be expressed as follows (Zhang et al., 2021).

$$[H]_{i,j,k} = u + \sum_{a=-\Delta}^{\Delta} \sum_{b=-\Delta}^{\Delta} \sum_{c=-\Delta}^{\Delta} [V]_{a,b,c} [X]_{i+a,j+b,k+c}$$
(9)

where, $[X]_{i,j,k}$ and $[H]_{i,j,k}$ represent the local porosity in 3-D space of input at location i, j, k and hidden layer, respectively; u is the bias; $[V]_{a,b,c}$ is the convolutional kernel, which represents the weights in the convolutional layer. The convolutional kernel performs the cross-correlation with input matrix, as it moves across the matrix X. The kernel shape and moving offsets, which are known as stripes, are hyperparameter in the CNNs model. Fig. 1 illustrates how the cross-correlation operation is applied to digital rock data in a layer-by-layer manner, to obtain the output value. The cross-correlation operation involves multiplying the values of the input matrix and the kernel matrix at each position and then summing up all the products, while kernel matrix slides through the input matrix. Fig. 1 (a) shows the examples of cross-correlation with different kernel size. In these examples, the $1 \times 1 \times 1$ kernel with value 2 multiplies to each value in the input matrix and generates the output matrix, while two matrices with the same dimensions generate a scale value. As shown in Fig. 1 (b), when the input matrix is multiplied by a zero kernel, it results in a matrix of zeros, whereas multiplication with a kernel with value 1 preserves the original input matrix. Fig. 1 (c) shows

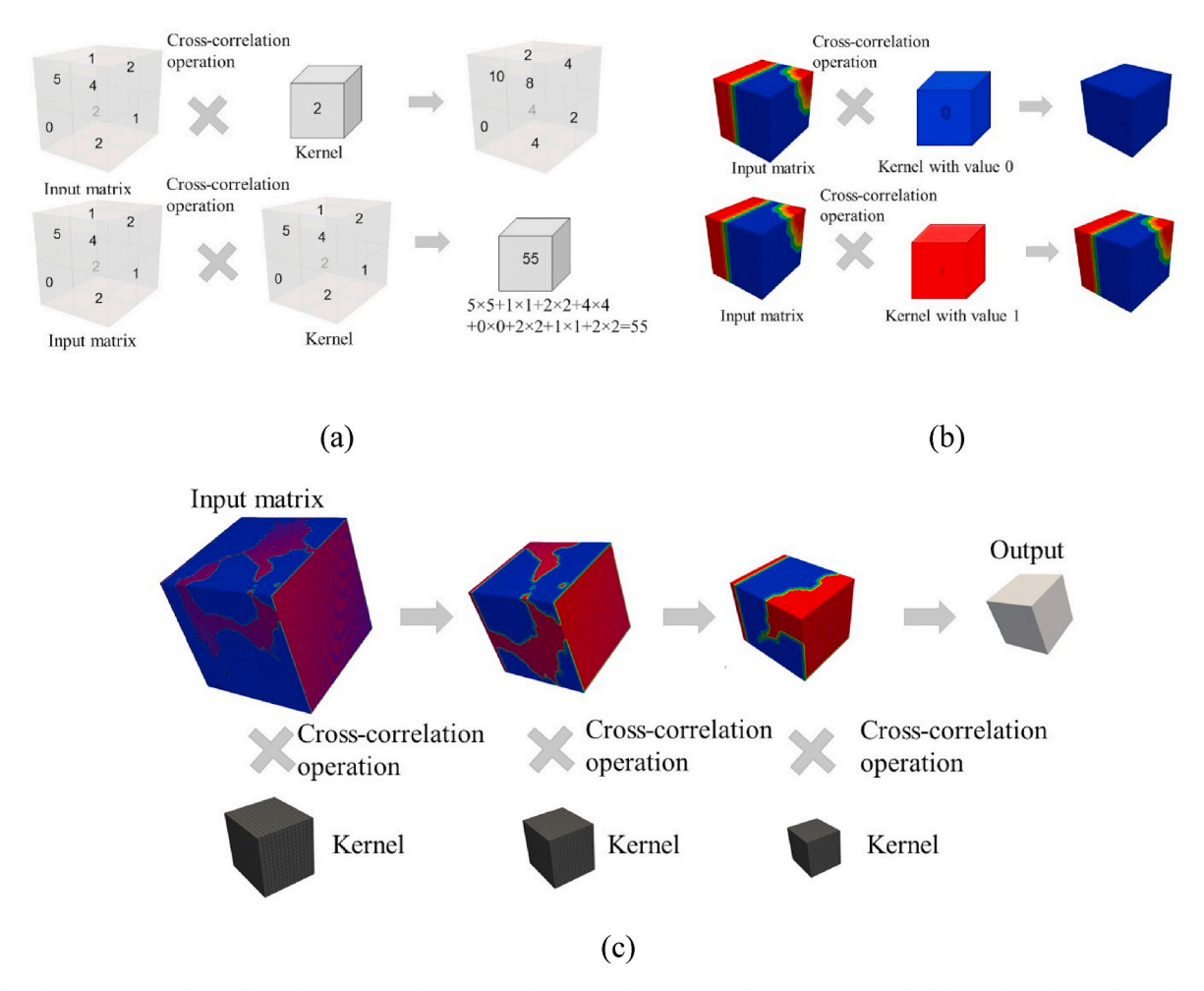


Fig. 1. The schematic of convolutional kernel performing the cross-correlation. (a) The cross-correlation operation with different kernel sizes; (b) implementation of cross-correlation on digital rock sample with zero kernel and one kernel; (c) process of cross-correlation to train kernels and obtain the output.

the implementation of cross-correlation between input matrix and kernel for several times. The dimension of the input matrix decreases gradually as generating the output. Consequently, by sliding the kernel and performing cross-correlation, features and patterns within the porous media's structure can be extracted and detected from the input data. In this study, this operation was implemented by using a 3-D matrix, representing the spatial distribution of microporous media. The left-hand side of the input matrix illustrates the extraction of local porosity of the digital rock image to a single output value through cross-correlation. When applying the CNNs method to train the model, the feature information of the digital rock is retained as a part of the convolutional kernel.

2.2.3. LeNet-5

Porous media exhibits spatial variations from the natural formation processes or structural variations within the material. Heterogeneity influences fluid flow and transport process, leading to preferential flow pathways or trapping of fluids within specific regions. In this regard, we applied LeNet to establish the model that can capture intricate patterns of porous media, efficiently model the complex interactions between input and output, and excellently perform on unseen data. LeNet is one of the CNN architecture proposed by LeCun et al. (1998). Due to its simple structure, LeNet has high efficiency when handling digital rock information. The input of LeNet is the spatial distribution of pores, and the output is permeability, effective surface area, and effective diffusion coefficient, respectively. We trained three LeNet models to predict each parameter. We compared several modern CNNs, including Residual

Networks (ResNet), AlexNet, and LeNet (He et al., 2016; LeCun et al., 1998). Among them, LeNet-5 is known to have the best performance on predicting permeability, effective surface area, and effective diffusion coefficient. We adapted LeNet-5, where the network was consisted of nine layers, as shown in Fig. 2. The adopted LeNet included CNN layers, average pooling layers, and fully connected layers. ReLU activation function was used to add non-linearity after every CNN layer. Then, average pooling layer was added in the network to reduce the individual noisy pixels, leading to a robust representation (Bashivan et al., 2022). We used five fully connected layers to extract and aggregate features.

The LeNet was adapted from PyTorch (Paszke et al., 2019), a machine learning framework based on the Torch library, and the model was trained by NVDIA V100 in Research Computing Data Core (RCDC) at University of Houston. The deep learning network was trained using the Adam optimizer (Kingma and Ba, 2014) to initialize the weights and biases for each neuron with the learning rate (i.e., relaxation coefficient) of 0.0001 for 500 epochs. The mean squared error (MSE) loss function was employed to measure the model's performance on the validation set, where the learning rate scheduler named ReduceLROnPlateau (Zaheer et al., 2018) was used to dynamically adjust the learning rate during the training procedure based on the validation loss. The training process utilized stochastic gradient descent (SGD) (Bottou, 2010) with back-propagation to update the model's parameters in the mini-batches of data with the size of 32 for each batch. The training set and test set contained three batches and one batch, respectively.

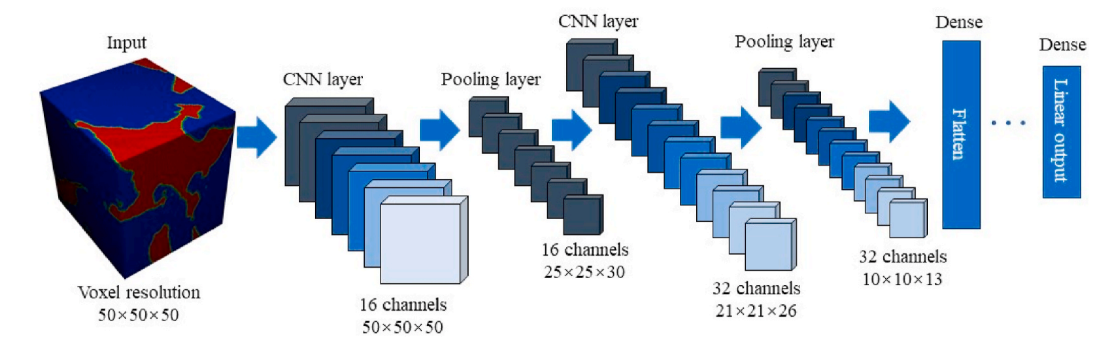


Fig. 2. The schematic of LeNet (LeCun et al., 1998).

2.3. Upscaling to continuum-scale simulation model

We utilized LeNet to train three deep learning models to predict the effective surface area, permeability, and effective diffusion coefficient, respectively, based on the given pore structures. The schematic workflow is illustrated in Fig. 3. The full-size digital rock, consisting of $800\times800\times800$ voxels, was subdivided into 4096 subvolumes, with the individual dimensions of $50\times50\times50$ voxels. For each subvolume, we employed the trained pore-scale models to estimate its averaged effective surface area, permeability, and effective diffusion coefficient. In the continuum-scale simulation model, the computational domain was discretized into the grid dimensions of $16\times16\times16$, where each grid cell corresponded to one subvolume within the entire digital rock.

The governing equations for the continuum-scale simulation is as follows. First, fluid flow in porous media is solved by Darcy's law to determine fluid pressure (*p*) as follows.

$$\mathbf{u} = -\frac{K}{\mu}(\nabla p - \rho g) \tag{10}$$

Second, following continuity equation is solved to determine porosity (φ) as follows.

$$\frac{\partial \varphi}{\partial t} + \nabla \bullet u = 0 \tag{11}$$

In this work, we used φ to describe the porosity in continuum-scale simulation and ε_f to describe the volume fraction of pore in pore-scale simulation. Third, following advection-diffusion equation is solved to address the concentration of species (C_f) as follows.

$$\frac{\partial(\varphi C_f)}{\partial t} + u \bullet \nabla C_f = \nabla \bullet (\varphi D_e \bullet \nabla C_f) - a_v k_c (C_f - C_s)$$
(12)

where, C_f is the concentration of species of reactants in aqueous phase, such as H^+ for acid dissolution problem; C_s is the concentration of acid at the fluid/solid interface; k_c is the coefficient of local mass transfer by reaction; a_v is the effective surface area for the mineral dissolution reaction; D_e is the effective diffusion coefficient of species. Reaction rate of mineral dissolution $(R(C_s))$ is described as follows.

$$R(C_s) = k_c (C_f - C_s) \tag{13}$$

In the first order reaction, reaction rate is determined as $R(C) = k_s C_s$, where k_s is the dissolution-rate constant. C_s is described as follows (Panga et al., 2005).

$$C_s = \frac{C_f}{\left(1 + \frac{k_s}{k_c}\right)} \tag{14}$$

By inserting Eq. (14) into Eq. (12), we obtain the following equation.

$$\frac{\partial(\varphi C_f)}{\partial t} + u \bullet \nabla C_f = \nabla \bullet \left(\varphi D_e \bullet \nabla C_f\right) - a_v k_s \frac{C_f}{\left(1 + \frac{k_s}{k_c}\right)}$$
(15)

Finally, the porosity-evolution equation is described as follows under the first-order reaction.

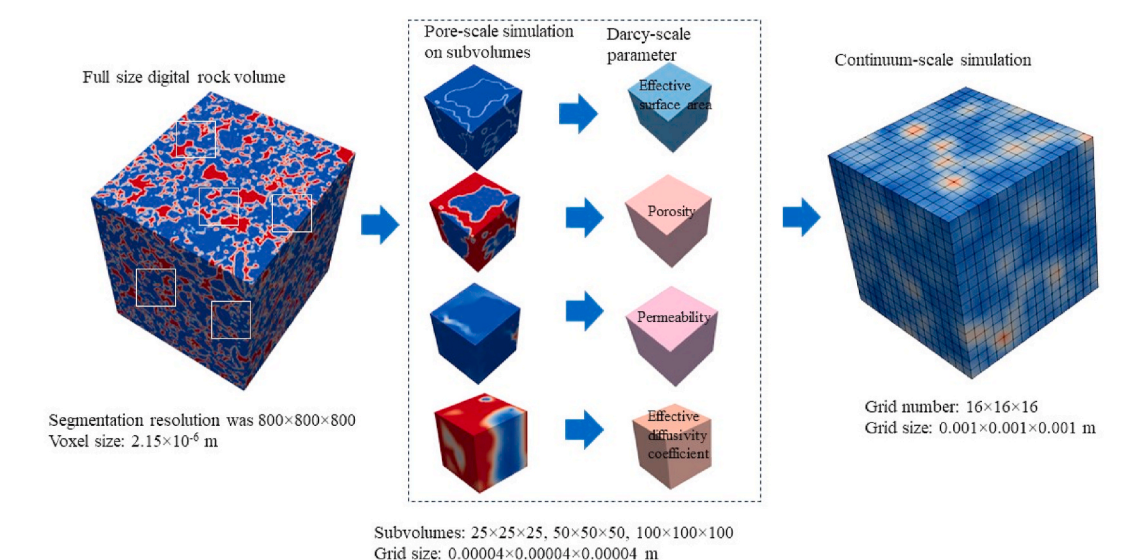


Fig. 3. The schematic of upscaling procedure from pore-scale simulation model to continuum-scale simulation model.

$$\frac{\partial \varepsilon}{\partial t} = \frac{R(C)a_{\nu}\alpha}{\rho_{\nu}} \tag{16}$$

where, α is the dissolving power, which is defined as grams of solid dissolved per mole of acid reacted (Panga et al., 2005). Here, local mass transfer coefficient (k_c) is obtained by the following correlation.

$$Sh = \frac{2k_c l}{D_m} = Sh_{\infty} + 0.8Re_p^{1/2} Sc^{1/3}$$
 (17)

where, Sh is the Sherwood number, which is defined by the ratio of convective mass transfer to diffusive mass transfer. Sh_{∞} is the asymptotic Sherwood number; Re_p is the Reynolds number defined by $Re_p = t^{\frac{2||u||l}{\nu}}$; Sc is the Schmidt number, which is defined by $Sc = \frac{\nu}{D_m}$; D_m is the molecular diffusivity; ν is the kinematic viscosity; l is the characteristic length, which we use pore radius. The pore radius can be quantified by:

$$\frac{r}{r_0} = \left[\frac{\varphi(1-\varphi_0)}{\varphi_0(1-\varphi)}\right]^{\beta} \tag{18}$$

where, r_0 is the initial mean pore size; β is the pore structure-relation constant.

In the application to the reactive transport problem, we assumed the linear relationship between permeability and effective surface area with respect to porosity during the mineral dissolution process as follows.

$$\frac{K}{K_0} = \frac{\varphi}{\varphi_0} \tag{19}$$

$$\frac{a_{v}}{a_{v0}} = \left(\frac{\varphi}{\varphi_{0}}\right)^{-1} \tag{20}$$

where, φ_0 is the initial porosity, K_0 is the initial field permeability, and a_{v0} is the initial field effective surface area, respectively.

3. Results and discussions

3.1. Pore-scale simulation results

The pore-scale simulation was implemented on 3-D sandstone digital rock images of the tomogram and segmentation of Bentheimer (BHG), Castlegate (CG), and Leopard Sandstones (LP) (Cui et al., 2022). Since the pore structures were highly heterogeneous, the predictive model could result in unsatisfactory results, if the training data was not sufficiently representative. Thus, to enhance the diversity of input data, we cut subvolumes into different scales for each type of digital rock. The subvolumes were selected randomly from the whole digital rock, and the subvolumes' voxels were in the wide range. The segmentation resolution was $800 \times 800 \times 800$ voxels; BHG and LP sandstone segmentations had the size of $2.15 \mu m/voxel$, while CG had the size of $3.4 \mu m/voxel$. In this study, the pore-scale model geometries (i.e., constituents of continuum-scale model) were made from the digital rock dataset, with three different cases of voxel dimensions of $25 \times 25 \times 25$, $50 \times 50 \times 50$. and $100 \times 100 \times 100$. For LP sample, we selected 22, 12, and 6 subvolumes at each size; for CG sample, we selected 20, 10, and 7 subvolumes at each dimension; for BHG sample, 19, 7, and 7 subvolumes were selected at each dimension. As such, the total subvolume case for training set was 110. The generated subvolumes were in high heterogeneity. Fig. 4 shows the heterogeneity presenting in our various 3-D subvolumes, with the examples of subvolumes consisting the full-size sample. The Python library netCDF4 (Unidata, 2012) was used to read segmentation information and the generated initial conditions for the pore-scale numerical simulations. The original segmentation of the digital rock image was comprised of five distinct phases: 1 denotes the macro-pore space; 2 denotes the clay; 3 denotes the quartz; 4 denotes the feldspar; 5 denotes the high-density minerals, respectively (Cui et al., 2022). In our simulation, we considered pore space filled with fluid phase and minerals with solid phase, respectively. The dimensions of the computational domain were 0.001 m \times 0.001 m \times 0.001 m for 25 \times 25 \times 25 cases, and 0.002 m \times 0.002 m \times 0.002 m for 50 \times 50 \times 50 cases, and 0.004 m \times 0.004 m \times 0.004 m for 100 \times 100 \times 100 cases, respectively. The input parameters for the simulation are listed in Table 1.

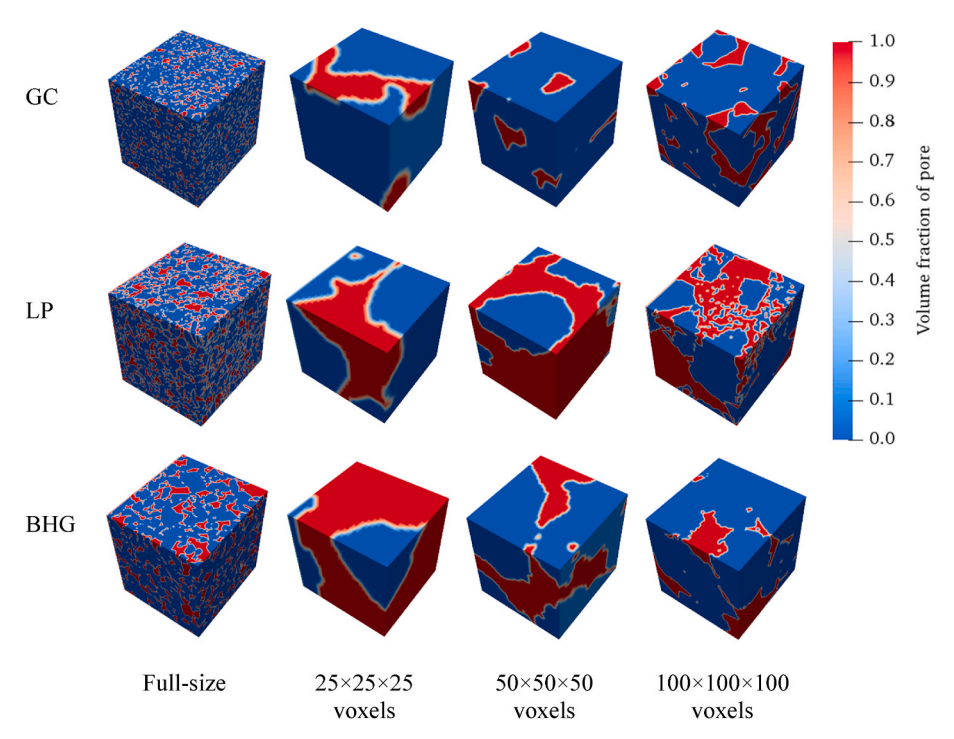


Fig. 4. Examples of subvolumes consisting the full-size digital rock.

Table 1The input parameters for the pore–scale modeling.

Parameter	Value
Inlet velocity	$1 \times 10^{-4} \text{ m/s}$
Diffusion coefficient of acid (reactant)	$1 \times 10^{-9} \text{ m}^2/\text{s}$
Fluid density	920 kg/m ³
Fluid viscosity	$2.4 \times 10^{-4} \text{ Pa} \bullet \text{s}$
Inlet concentration of acid	0.5 wt%

The pore-scale simulation describing the fluid flow and transport phenomena was implemented on the subvolumes. Fig. 5 shows the simulation results of porosity and effective surface area for each subvolumes. Porosity and effective surface area within each subvolume were computed as the volumetric averages of pore volume fraction and effective surface area of discrete grid blocks. The porosity values spanned a wide range from 0.1 to 0.887. Notably, the subvolume with the smallest porosity corresponded to the 25 \times 25 \times 25-CG case, while the largest porosity emerged from the 25 \times 25 \times 25-BHG case. 25 \times 25 \times 25 subvolume cases exhibited a comparatively broader porosity distribution compared to $100 \times 100 \times 100$ subvolume cases. Furthermore, 25 \times 25×25 resolution cases displayed a wider distribution of effective surface areas. This observation suggests that incorporating a substantial number of $25 \times 25 \times 25$ resolution cases in the training set enabled the comprehensive coverage of porosity and effective surface area values. Thus, the model could achieve convergence more easily while avoiding the overfitting by taking the wide range of input datasets. From the distribution of porosity and effective surface area, we could observe that the effective surface area was relatively small under high (>0.5) and low (<0.3) value of porosity. Under the intermediate values of porosity (0.3-0.5), the effective surface area was relatively high in the same subvolumes. This is because, the effective surface was related not only to the porosity, but also to the structure and grain arrangement. Under high porosity, there were more voids or interconnection within the media, and the solid surface area was relatively low. Under low porosity, the media had dense structure, which led to smaller solid surface area. However, the relationship between the effective surface area and porosity does not necessarily follow a trend. If the porous media has a complex, convoluted, or highly branched structure, effective surface area can be large despite with low porosity.

Fig. 6 presents the computed porosity and permeability of simulated cases. The permeability ranged from 1.41 \times 10^{-14} m 2 1.79 \times 10^{-7} m 2 .

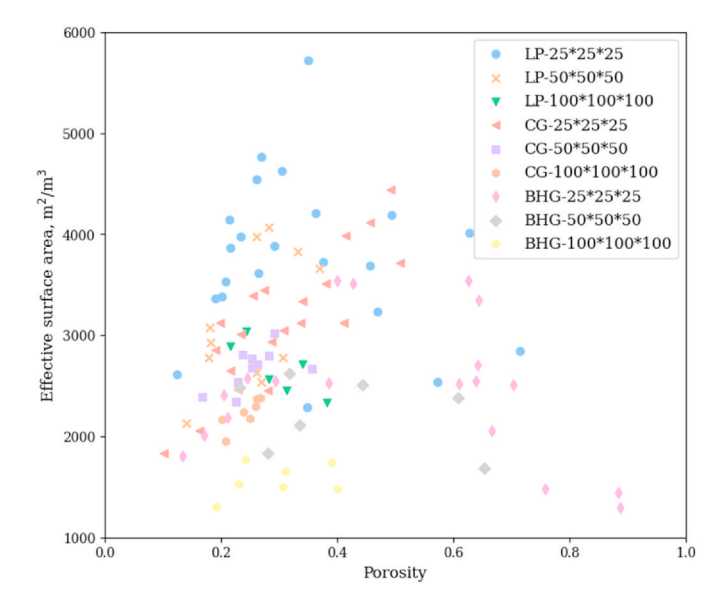


Fig. 5. Porosity and effective surface area obtained from the pore-scale simulation of fluid transport using various subvolumes.

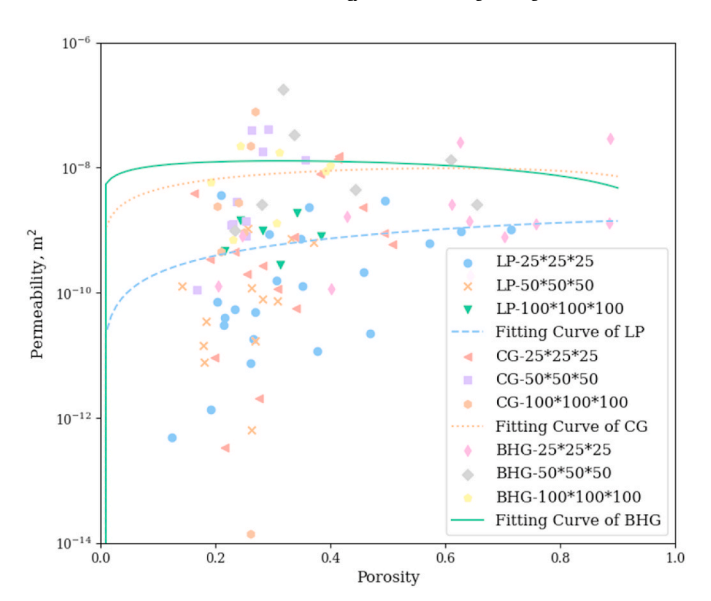


Fig. 6. Porosity and permeability obtained from the pore-scale simulation of fluid transport using various subvolumes.

The trend was similar with the published relationship of porosity and permeability (Bohnsack et al., 2020; Wei et al., 2015). We used Kozeny-Carman porosity-permeability relationship to be matched with the obtained distribution of porosity and permeability, which has the following relationship.

$$K = C \frac{\varphi^{m+1}}{(1 - \varphi)^m} \tag{21}$$

where, C is the Kozeny coefficient, and m is the Archie exponent (Costa, 2006). The values of C, m, and corresponding R^2 are listed in Table 2.

As such, low values of R² were observed when Kozeny-Carman relationship model was used to be fitted with the computed data of porosity and permeability. It shows the difficulty of approximating the porosity and permeability relationship with a single function, under the complexity of pore structures and significant heterogeneity. Thus, we considered an advanced deep learning method to predict the porosity and permeability relationship, as taking the pore structure and heterogeneity into account. Obtained porosity and permeability relationship would be used as input data for the continuum-scale modeling.

To quantify the diffusion behavior of reactant (i.e., acid) within the porous media in the continuum-scale model, effective diffusion coefficient was computed through the pore-scale modeling. Fig. 7 shows the method of determining the effective diffusion coefficient with pore-scale and continuum-scale simulations. To obtain the continuum-scale simulation parameter of effective diffusion coefficient, we simulated the acid diffusion in 3-D pore-scale model, obtained the breakthrough curve at the outlet of the domain, and matched the breakthrough curve with the result from pseudo-one-dimensional diffusion. The pseudo-one-dimensional diffusion simulation was conducted with the same dimension (i.e., length, height, and width) of computational domain as the 3-D pore-scale simulation. We discretized the domain into $35 \times 1 \times 1$ meshes to conduct pseudo-one-dimensional diffusion simulation. Effective diffusion coefficient is a continuum-scale parameter to describe the diffusion phenomena as the obstruction in diffusion

Table 2 Values of *C*, *m*, and R² of the fitting with Kozeny-Carman relationship.

Sample	С	m	\mathbb{R}^2
LP CG	1.79×10^{-9} 1.91×10^{-8}	0.94 0.61	0.075 0.013
BHG	2.38×10^{-8}	0.31	0.013

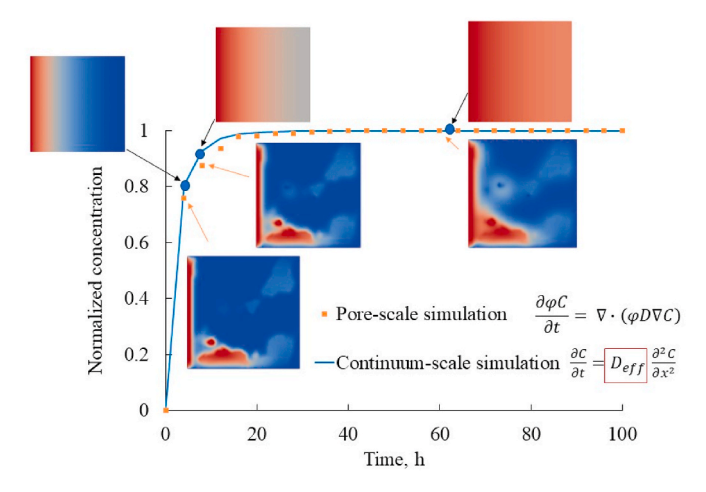


Fig. 7. Schematic graph to illustrate the process of finding effective diffusion coefficients.

imposed by porous media's structures (El Oualid et al., 2017). Thus, by matching the breakthrough curve from pore-scale models and the result from one-dimensional diffusion simulation (Deng et al., 2021), we could find the corresponding effective diffusion coefficient that represented the diffusion influenced by the pore-scale structure.

Here, the governing equation for the tracer experiment on the ideal grain pore-scale models is described as follows.

$$\frac{\partial \varphi C}{\partial t} = \nabla \bullet (\varphi D \nabla C) \tag{22}$$

where, *D* is the effective diffusion coefficient in pore-scale. The diffusion of acid in the continuum-scale model can be described by the following Fick's Law under the transient condition.

$$\frac{\partial C}{\partial t} = D_{eff} \frac{\partial^2 C}{\partial x^2} \tag{23}$$

where, D_{eff} is the effective diffusion coefficient in continuum-scale. In order to find D_{eff} of the corresponding pore structure, we needed to adjust D_{eff} in continuum-scale simulation to match the breakthrough curve with the pore-scale simulation results. To find D_{eff} , we first obtained the breakthrough curve from pore-scale simulation. Then, we set different D_{eff} in Eq. (23) until the mean squared error (MSE) between

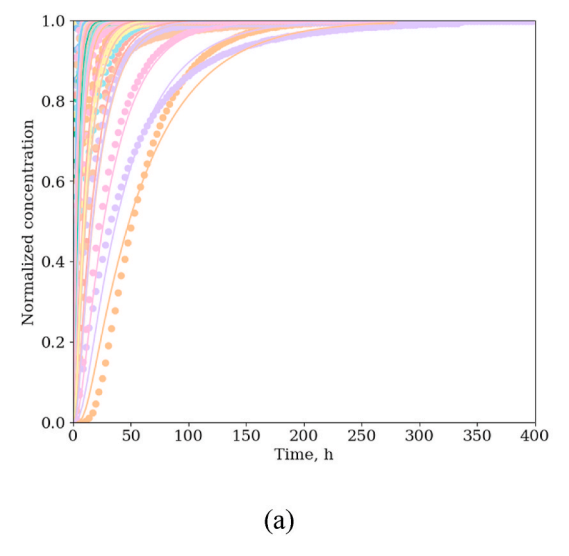
pore-scale breakthrough curve and continuum-scale breakthrough curve was less than the given criteria. Eq. (23) was solved by OpenFOAM solver, scalarTransportFoam (Weller et al., 1998). Python library PyFoam (Gschaider et al.) provided the application programming interface to execute OpenFOAM simulation in Python code. The pseudo-one-dimensional diffusion simulation had the same computational domain, grid size, time step, and inlet concentration as the pore-scale simulation. The top and bottom walls in the pore-scale model were set as coupled cyclic boundary, and the cell value at boundary was set equal to the adjacent pair of cyclic patches. To be specific, the matching process started from the initial value of D_{eff} , and then added a searching step to obtain the concentration (C) distribution. With every Deff, breakthrough curve calculated by concentration was compared with the pore-scale breakthrough curve until their MSE satisfied the criteria of 0.01. When MSE calculated by the concentration at the outlet boundary between pore-scale simulation and continuum-scale simulation reached the criteria, the effective diffusion coefficient was considered as identified. Otherwise, the search process continued. In this study, we searched the effective diffusion coefficient from $5\times 10^{-12}\,\text{to}$ 5×10^{-9} m²/s with the searching step of 2×10^{-13} m²/s.

Fig. 8 (a) shows the computed results of effective diffusion coefficients. The scattered dot-curves were obtained from the pore-scale diffusion simulation, and the solid lines were continuum-scale breakthrough curve obtained as the above-mentioned method. The normalized concentration was the average concentration at the outlet boundary divided by the input concentration. Fig. 8 (b) shows the relationship of porosity and effective diffusion coefficient. With the increasing porosity, effective diffusion coefficient decreased and exhibited a wide range.

Fig. 9, Fig. 10, and Fig. 11 show the velocity streamlines, pore structure, and distribution of concentration of acid with respect to time, respectively. Fig. 9 was obtained with 25 \times 25 \times 25 resolution case of CG_07; Fig. 10 was obtained with 50 \times 50 \times 50 resolution case of LP_08; Fig. 11 was obtained with 100 \times 100 \times 100 resolution case of BHG_05, respectively. Acid flowed into the system through the velocity streamlines, gradually diffused into the pore space, and its concentration distribution reached the equilibrium status at the time of about 800 s.

3.2. Deep learning modeling

We trained the CNNs deep learning model by taking the pore structures as the input data and the pore-scale simulation results as the output data, respectively. During the training process, MSE converged to the magnitude of 10^{-4} . We trained the models to predict the effective



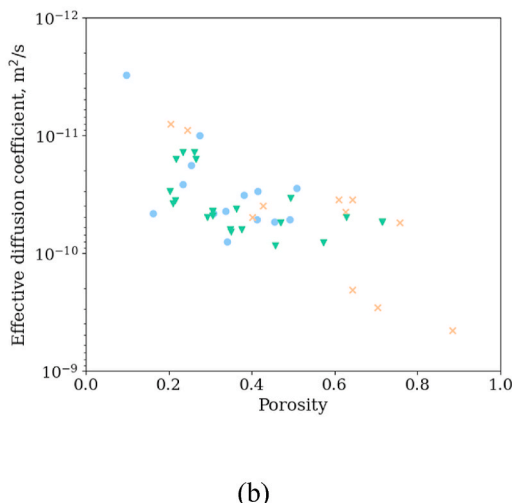


Fig. 8. (a) Breakthrough curves of comparison between pore-scale simulation (scattered-dots) with 1-D diffusion; (b) relationship between porosity and effective diffusion coefficient.

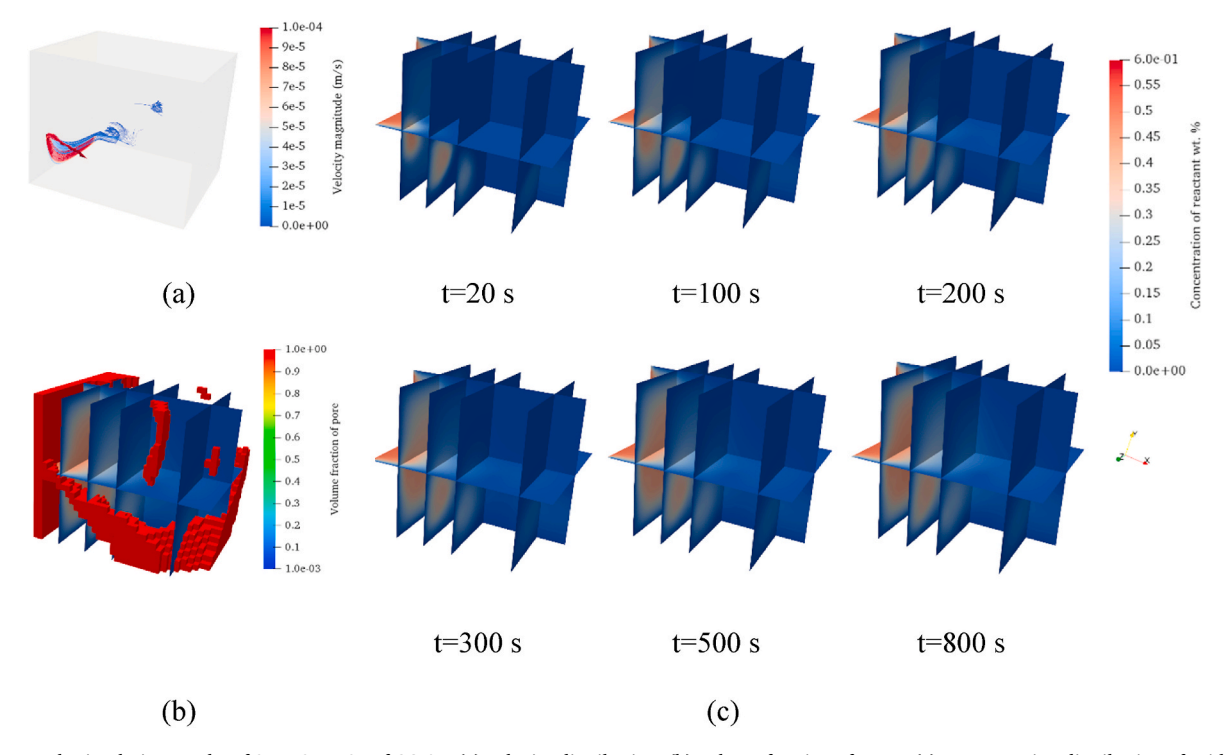


Fig. 9. Pore-scale simulation results of $25 \times 25 \times 25$ of CG_07, (a) velocity distribution; (b) volume fraction of pores; (c) concentration distribution of acid at t=20, 100, 200, 300, 500, and 800 s.

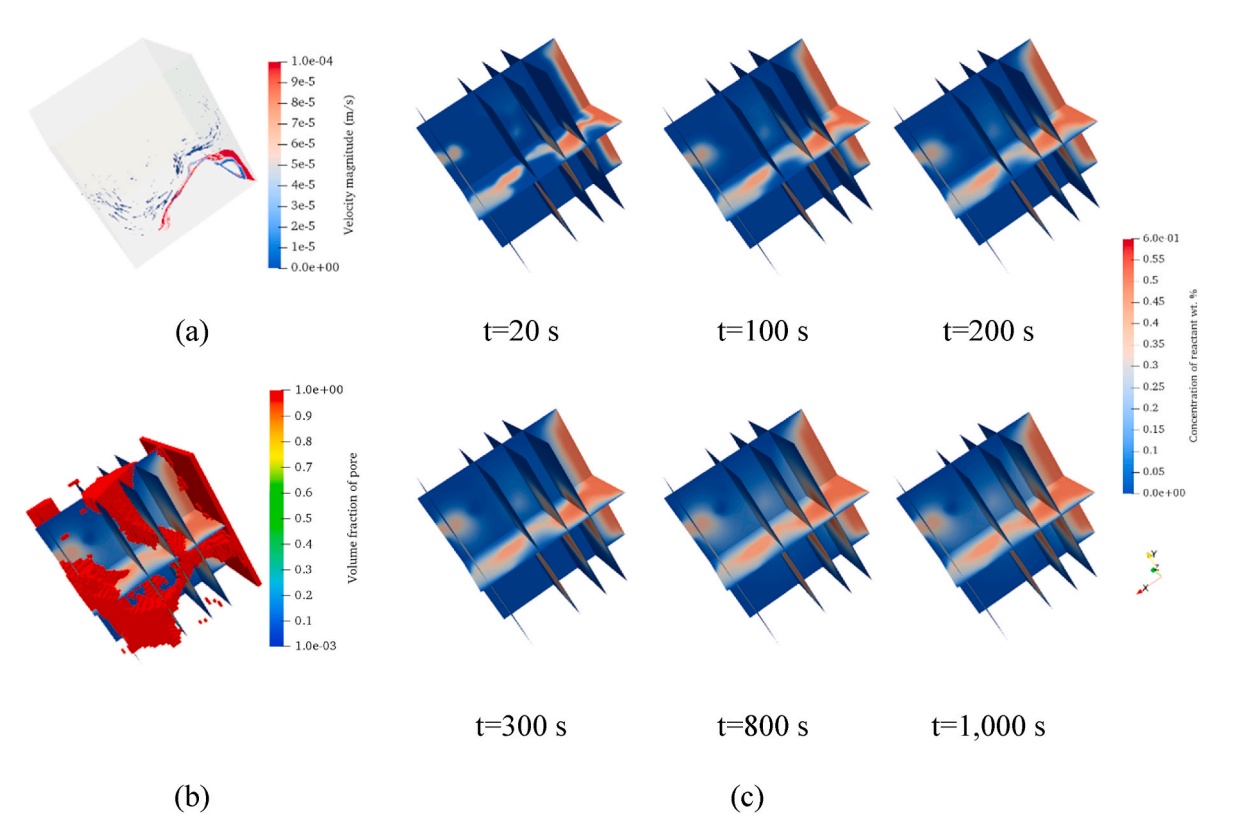


Fig. 10. Pore-scale simulation results of $50 \times 50 \times 50$ case of LP_08, (a) velocity distribution; (b) volume fraction of pore; (c) concentration distribution of acid at t = 20, 100, 200, 300, 800, and 1000 s.

surface area, permeability, and effective diffusion coefficient, which would be used as the input parameters of continuum-scale modeling of mineral dissolution. MSE of training set was provided in Fig. 12. During the training process, MSE on training set was smaller than 0.005. The

model reached convergence within 100 epochs. When we applied the model on test set, MSE on test set was less than 0.3.

Fig. 13 compares the predicted results by the deep learning models with the label data (i.e., output data, which is the real values of pore-

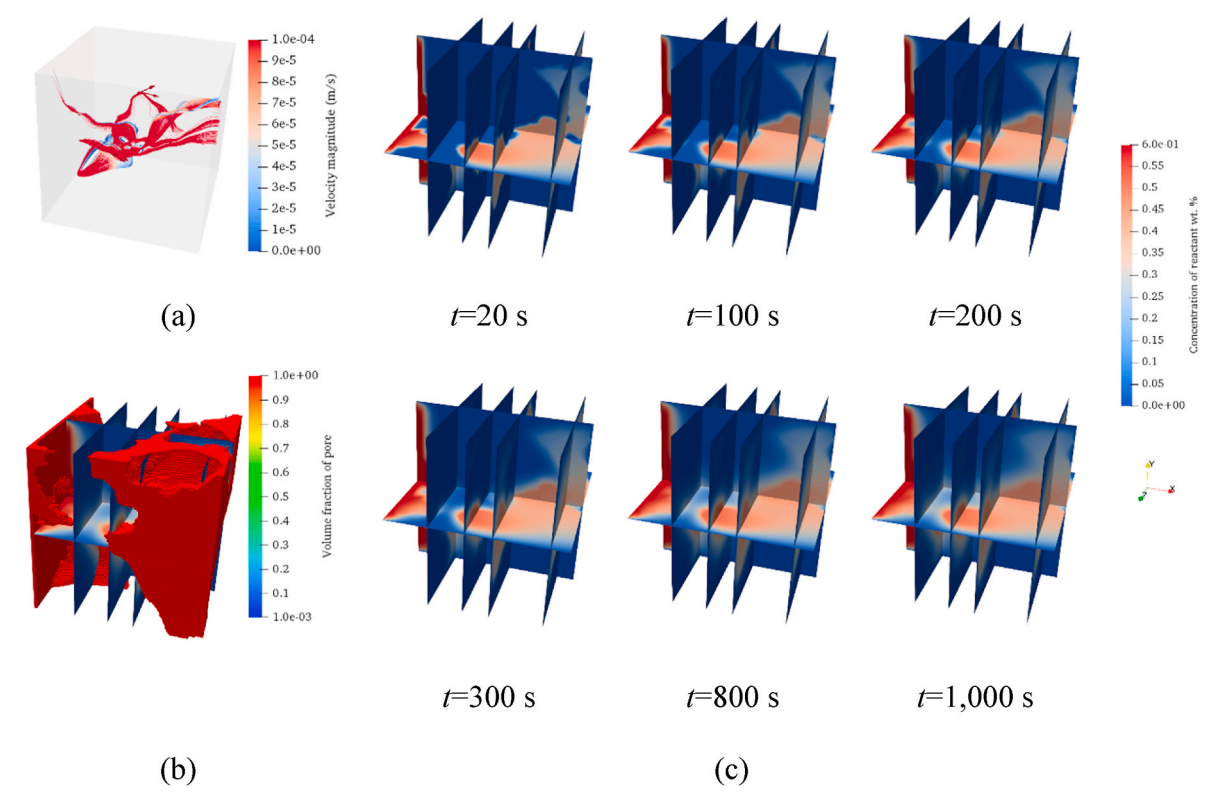


Fig. 11. Pore-scale simulation results of $100 \times 100 \times 100$ case of BHG_05, (a) velocity distribution; (b) volume fraction of pore; (c) concentration distribution of acid at $t=20,\,100,\,200,\,300,\,800$, and 1000 s.

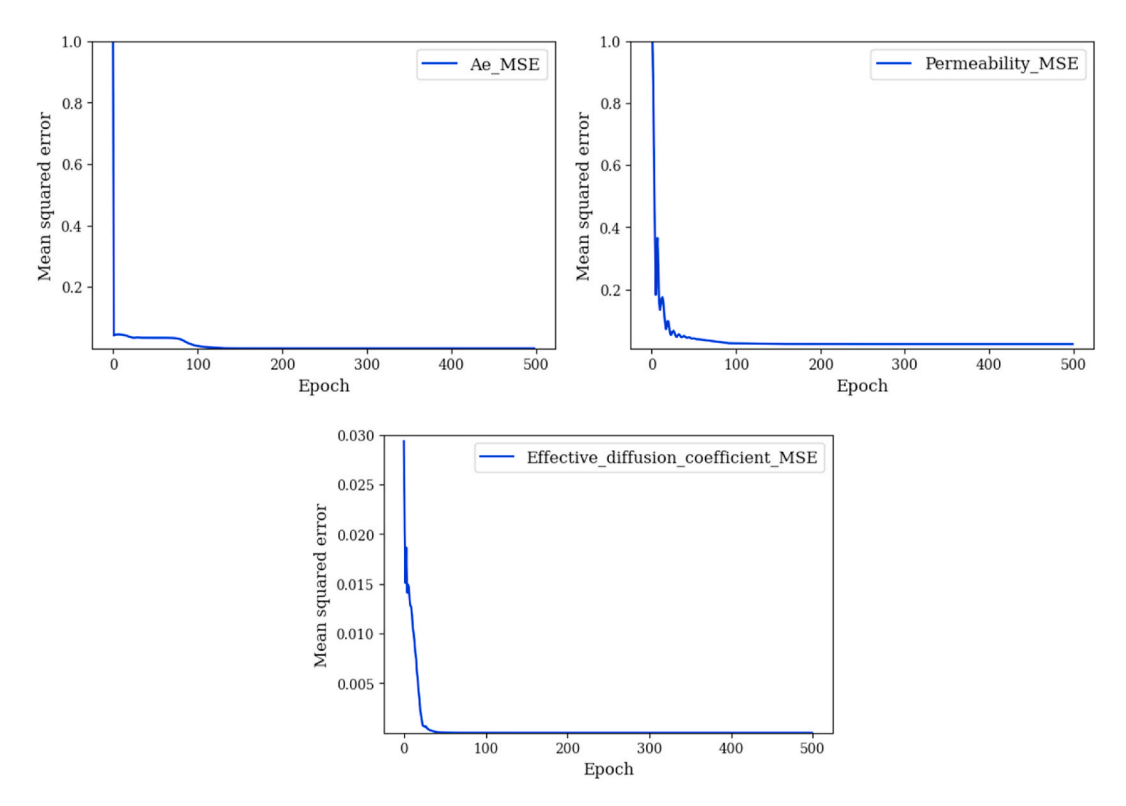


Fig. 12. MSE during training.

scale modeling results), which included the effective surface area, permeability, and effective diffusion coefficient. The MSE between the predicted values and the real values of effective surface area, permeability, and effective diffusion coefficient were 0.23, 0.18, and 0.0076,

respectively. Among them, effective diffusion coefficient showed lowest MSE, which could be caused by the narrow range of the label data. The effective surface area and permeability exhibited a broad and evenly distributed range, resulting in a representative distribution that

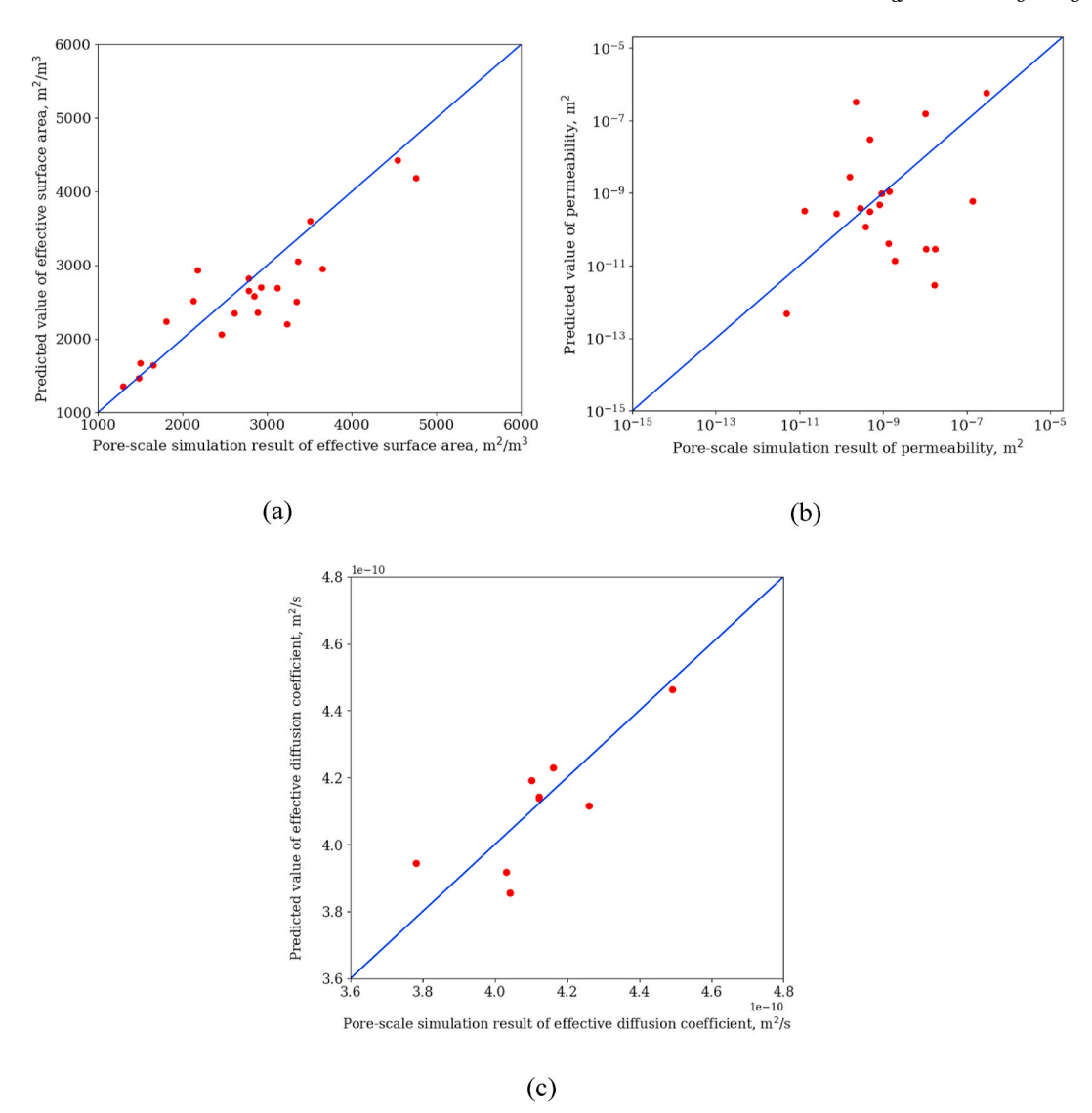


Fig. 13. Comparison of predicted results by the deep learning models with the real values of pore-scale modeling results. (a) Effective surface area; (b) permeability; (c) effective diffusion coefficient.

accurately captured the diverse characteristics of the pore structure. These distributions of the output parameters reflect a high level of variability and provide a reliable representation of the complex nature of the pore structures, as allowing us to reliably predict the continuum-scale parameters with the given pore structures.

3.3. Continuum-scale simulation results

We obtained the porosity (φ_0), permeability (K_0), effective surface area (a_{v0}), and effective diffusion coefficient (D_{eff}) from the full-size digital rock volume, and applied them to the continuum-scale simulations. The computational domain for the continuum-scale simulation had the domain size of 0.016 m \times 0.016 m \times 0.016 m, with the grid number of $16 \times 16 \times 16$. The grid size (i.e., 0.001 m) was equal to the domain size of the pore-scale models. The input parameters for the continuum-scale simulation of mineral dissolution by acid is listed in Table 3. We set the fixed velocity, pressure, and acid concentration at the inlet boundary. The outlet boundary for velocity, pressure, and acid concentration field was set as zero gradient. The simulation results of the profiles of concentration distribution of acid, porosity, and effective surface area are presented in Fig. 14. As acid flowed into the domain, the dissolution reaction altered the porosity and the pore distributions. The

Table 3Input parameters for the continuum-scale simulations, which were obtained with the deep learning models.

Parameter	Symbol	Value
Acid diffusivity	D_m	$1 \times 10^{-9} \text{m}^2/\text{s}$
Dissolving power	α	50 kg/kmol
Asymptotic Sherwood number	Sh_{∞}	3.66
Pore-structure-relation constant	β	1
Rock density	$\rho_{\rm s}$	2710 kg/m^3
Dynamic viscosity	μ	0.001 kg/m·s
Reaction rate constant	k_s	0.002 m/s
Inlet velocity	u	0.0001 m/s
C_f	Inlet concentration	4 wt%

dissolution pattern followed the conical dissolution (Fredd and Fogler, 1999). The initial parameters such as permeability, effective surface area, and effective diffusion coefficients were obtained from deep learning models, which implied the information of pore structure and heterogeneity without the heavy computational expenses. As such, the presented upscaling method based on deep learning technology can be applied to effectively improve the computational efficiency.

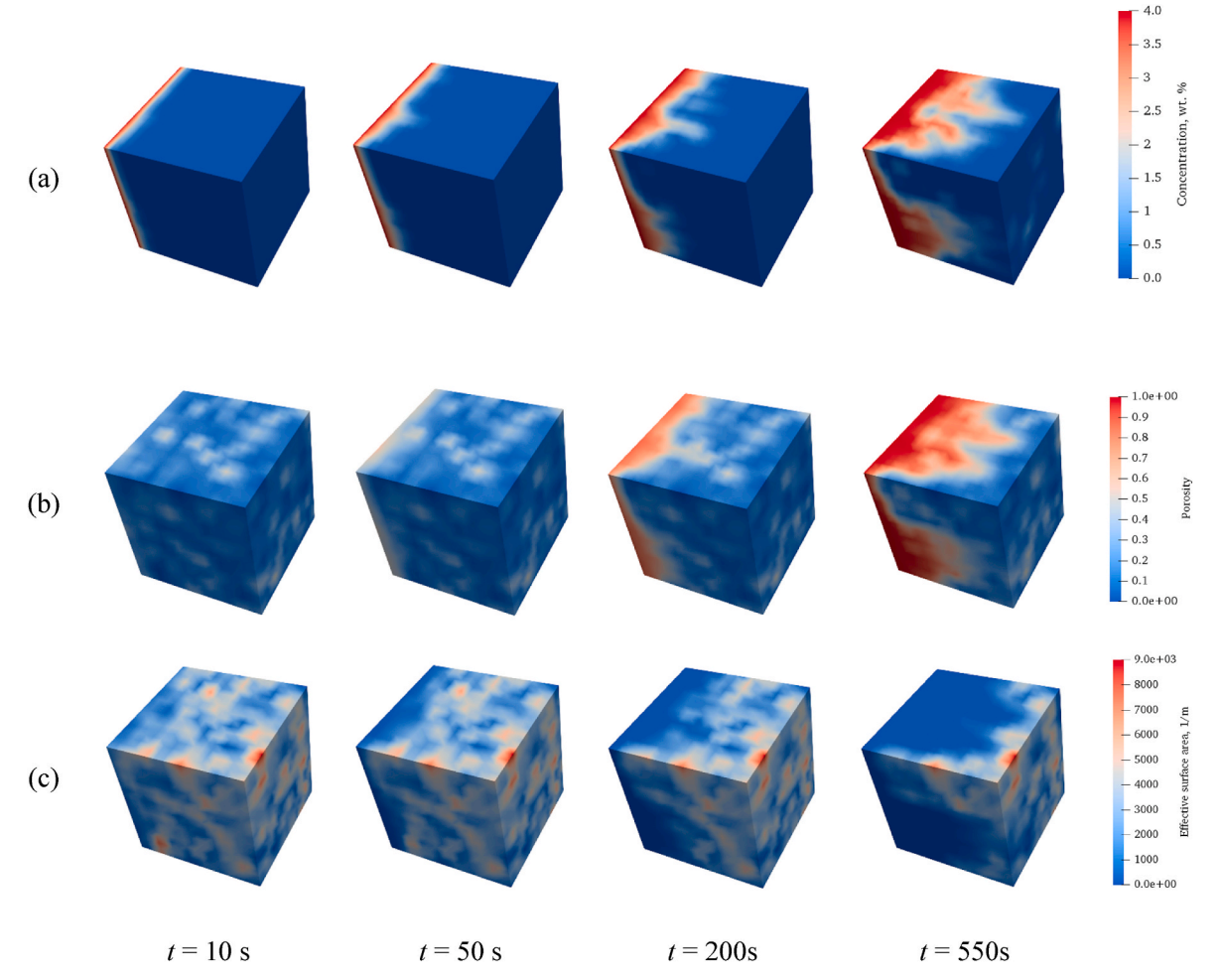


Fig. 14. Continuum-scale simulation results of (a) concentration distribution of acid; (b) porosity; (c) effective surface area.

4. Conclusion

Reactive transport modeling of subsurface systems can help address various geochemical processes, such as dissolution and precipitation of minerals. Accurate prediction of key reactive transport properties is critical in understanding such subsurface phenomena. However, there are challenges to efficiently and reliably compute the solutions of complex reactive transport problems, due to the high heterogeneity and intricate and irregular structures of subsurface porous media. In addition, transport models of porous media are in various scales spanning from pore-scale to continuum-scale and require reliable upscaling techniques to establish the connection between these models. In this regard, we established an upscaling method connecting pore-scale and continuum-scale models by employing a deep learning methodology of Convolutional Neural Networks (CNNs). In the pore-scale modeling, we applied the DBS method to simulate the fluid transport in pore-scale models, which acted as the constituents of a continuum-scale model. The obtained pore-scale modeling results were used to train the CNNs deep leaning models. The input data were consisted of the spatial distributions and structures of micropores, while the output data for the deep learning models include the permeability, effective surface area, and effective diffusion coefficient of each subvolume. These output data of the deep learning model was utilized as the input parameters for the continuum-scale reactive transport modeling of mineral dissolution. The workflow of this study presents the robust upscaling process, as connecting the insights obtained from pore-scale modeling to the input parameters of continuum-scale modeling.

CNNs-based upscaling method from pore-scale to continuum-scale

simulations offers the great computational efficiency and enhanced reliability in predicting reactive transport phenomena in porous media. The trained model can predict the key parameters immediately, which is expected to serve as a robust tool for optimizing reservoir management strategies, especially with time-sensitive decision making. Given that major limitations of supervised learning models include the unpredictable performance on unseen data and lengthy computational time for data training, the envisioned works will include the establishment of generalized database for variety of digital rock images in various repositories through computationally-efficient training.

CRediT authorship contribution statement

Jiahui You: Conceptualization, Data curation, Formal analysis, Investigation, Methodology, Validation, Visualization, Writing – original draft. **Kyung Jae Lee:** Funding acquisition, Project administration, Resources, Software, Supervision, Writing – review & editing.

Declaration of competing interest

The authors declare that they have no known competing financial interests or personal relationships that could have appeared to influence the work reported in this paper.

Data availability

Data will be made available on request.

Acknowledgement

We appreciate the funding for this research from National Science Foundation under Award 2042504 (CAREER: Identifying a New Source of Lithium for Sustainable and Renewable Energy Storage).

References

- Albawi, S., Mohammed, T.A., Al-Zawi, S., 2017. Understanding of a convolutional neural network. In: 2017 International Conference on Engineering and Technology (ICET). Ieee, pp. 1–6.
- Algive, L., Bekri, S., Lerat, O., Fadi, N., Vizika, O., 2009. Reactive Pore Network Modeling technology to evaluate the impact of diagenesis on the petrophysical properties of a rock. In: International Petroleum Technology Conference. International Petroleum Technology Conference, Doha, Qatar, p. 10.
- Alqahtani, N., Alzubaidi, F., Armstrong, R.T., Swietojanski, P., Mostaghimi, P., 2020. Machine learning for predicting properties of porous media from 2d X-ray images. J. Petrol. Sci. Eng. 184, 106514.
- Bashivan, P., Ibrahim, A., Dehghani, A., Ren, Y., 2022. Learning robust kernel ensembles with kernel average pooling. arXiv preprint arXiv:2210.00062.
- Bohnsack, D., Potten, M., Pfrang, D., Wolpert, P., Zosseder, K., 2020.

 Porosity-permeability relationship derived from Upper Jurassic carbonate rock cores to assess the regional hydraulic matrix properties of the Malm reservoir in the South German Molasse Basin. Geoth. Energy 8 (1), 12.
- Bottou, L., 2010. Large-scale machine learning with stochastic gradient descent. In: Proceedings of COMPSTAT 2010: 19th International Conference on Computational StatisticsParis France, August 22-27, 2010 Keynote, Invited and Contributed Papers. Springer, pp. 177–186.
- Costa, A., 2006. Permeability-porosity relationship: a reexamination of the Kozeny-Carman equation based on a fractal pore-space geometry assumption. Geophys. Res. Lett. 33 (2).
- Cui, Y.a.A., Christoph, Shikhov, Igor, 2022. 3D sandstone sample images. Digital Rocks Portal.
- Deng, H., Tournassat, C., Molins, S., Claret, F., Steefel, C.I., 2021. A pore-scale investigation of mineral precipitation driven diffusivity change at the column-scale. Water Resour. Res. 57 (5), e2020WR028483.
- Dormieux, L., Lemarchand, E., 2001. Homogenization approach of advection and diffusion in cracked porous material. J. Eng. Mech. 127 (12), 1267–1274.
- El Oualid, S., Lachat, R., Candusso, D., Meyer, Y., 2017. Characterization process to measure the electrical contact resistance of Gas Diffusion Layers under mechanical static compressive loads. Int. J. Hydrogen Energy 42 (37), 23920–23931.
- Estermann, S.-J., Scheiner, S., 2018. Multiscale modeling provides differentiated insights to fluid flow-driven stimulation of bone cellular activities. Frontiers in Physics 6, 76.
- Fredd, C.N., Fogler, H., 1999. Optimum conditions for wormhole formation in carbonate porous media: influence of transport and reaction. SPE J. 4 (3), 196–205.
- Gschaider, B. et al., PyFoam, pp. https://pypi.org/project/PyFoam/..
- He, K., Zhang, X., Ren, S., Sun, J., 2016. Deep residual learning for image recognition. In: Proceedings of the IEEE Conference on Computer Vision and Pattern Recognition, pp. 770–778.
- Hung, K.M., Hill, A.D., Sepehrnoori, K., 1989. A mechanistic model of wormhole growth in carbonate matrix acidizing and acid fracturing. J. Petrol. Technol. 41 (1), 59–66.
- Kingma, D.P., Ba, J., 2014. Adam: a method for stochastic optimization. arXiv preprint arXiv:1412.6980.
- LeCun, Y., Bottou, L., Bengio, Y., Haffner, P., 1998. Gradient-based learning applied to document recognition. Proc. IEEE 86 (11), 2278–2324.
- Lichtner, P.C., Kang, Q., 2007. Upscaling pore-scale reactive transport equations using a multiscale continuum formulation. Water Resour. Res. 43 (12).
- Liu, M., Kwon, B., Kang, P.K., 2022. Machine learning to predict effective reaction rates in 3D porous media from pore structural features. Sci. Rep. 12 (1), 5486.
- Liu, M., Mostaghimi, P., 2018. Reactive transport modelling in dual porosity media. Chem. Eng. Sci. 190, 436–442.
- Liu, M., Shabaninejad, M., Mostaghimi, P., 2017. Impact of mineralogical heterogeneity on reactive transport modelling. Comput. Geosci. 104, 12–19.
- Liu, M., Starchenko, V., Anovitz, L.M., Stack, A.G., 2020. Grain detachment and transport clogging during mineral dissolution in carbonate rocks with permeable grain boundaries. Geochem. Cosmochim. Acta 280, 202–220.
- Liu, M., Zhang, S., Mou, J., Zhou, F., 2013. Wormhole propagation behavior under reservoir condition in carbonate acidizing. Transport Porous Media 96 (1), 203–220.

- Maheshwari, P., Maxey, J., Balakotaiah, V., 2016. Reactive-dissolution modeling and experimental comparison of wormhole formation in carbonates with gelled and emulsified acids. SPE Prod. Oper. 31 (2), 103–119.
- Maheshwari, P., Ratnakar, R.R., Kalia, N., Balakotaiah, V., 2013. 3-D simulation and analysis of reactive dissolution and wormhole formation in carbonate rocks. Chem. Eng. Sci. 90, 258–274.
- Menke, H.P., Maes, J., Geiger, S., 2021. Upscaling the porosity–permeability relationship of a microporous carbonate for Darcy-scale flow with machine learning. Sci. Rep. 11 (1), 1–10.
- Minto, J.M., Lunn, R.J., El Mountassir, G., 2019. Development of a reactive transport model for field-scale simulation of microbially induced carbonate precipitation. Water Resour. Res. 55 (8), 7229–7245.
- Molins, S., et al., 2020. Simulation of mineral dissolution at the pore scale with evolving fluid-solid interfaces: review of approaches and benchmark problem set. Comput. Geosci. 25, 1285–1318.
- Moukalled, F., et al., 2016. The Finite Volume Method. Springer.
- Murtagh, F., 1991. Multilayer perceptrons for classification and regression. Neurocomputing 2 (5-6), 183–197.
- Oliveira, T.D.S., Blunt, M.J., Bijeljic, B., 2019. Modelling of multispecies reactive transport on pore-space images. Adv. Water Resour. 127, 192–208.
- Panga, M.K.R., Ziauddin, M., Balakotaiah, V., 2005. Two-scale continuum model for simulation of wormholes in carbonate acidization. AIChE J. 51 (12), 3231–3248.
- Paszke, A., et al., 2019. Pytorch: an imperative style, high-performance deep learning library. Adv. Neural Inf. Process. Syst. 32.
- Pivonka, P., Hellmich, C., Smith, D., 2004. Microscopic effects on chloride diffusivity of cement pastes—a scale-transition analysis. Cement Concr. Res. 34 (12), 2251–2260.
- Prasianakis, N.I., et al., 2020. Neural network based process coupling and parameter upscaling in reactive transport simulations. Geochem. Cosmochim. Acta 291, 126–143.
- Ratnakar, R.R., Kalia, N., Balakotaiah, V., 2013. Modeling, analysis and simulation of wormhole formation in carbonate rocks with in situ cross-linked acids. Chem. Eng. Sci. 90, 179–199.
- Röding, M., Ma, Z., Torquato, S., 2020. Predicting permeability via statistical learning on higher-order microstructural information. Sci. Rep. 10 (1), 15239.
- Sharma, S., Sharma, S., Athaiya, A., 2017. Activation functions in neural networks. Data Sci. 6 (12), 310–316.
- Soulaine, C., Roman, S., Kovscek, A., Tchelepi, H.A., 2017. Mineral dissolution and wormholing from a pore-scale perspective. J. Fluid Mech. 827, 457–483.
- Soulaine, C., Tchelepi, H.A., 2016. Micro-continuum approach for pore-scale simulation of subsurface processes. Transport Porous Media 113 (3), 431–456.
- Tahmasebi, P., Kamrava, S., Bai, T., Sahimi, M., 2020. Machine learning in geo-and environmental sciences: from small to large scale. Adv. Water Resour. 142, 103619.
- Unidata, 2012. Integrated data viewer (IDV) version 3.1. Boulder, CO: UCAR/Unidata [software].
- Wang, M., Wang, J., Pan, N., Chen, S., 2007. Mesoscopic predictions of the effective thermal conductivity for microscale random porous media. Phys. Rev. 75 (3), 036702.
- Wei, D.-F., Liu, X.-P., Hu, X.-X., Xu, R., Zhu, L.-L., 2015. Estimation of permeability from NMR logs based on formation classification method in tight gas sands. Acta Geophys. 63 (5), 1316–1338.
- Weller, H.G., Tabor, G., Jasak, H., Fureby, C., 1998. A tensorial approach to computational continuum mechanics using object-oriented techniques. Comput. Phys. 12 (6), 620–631.
- Wu, H., Fang, W.-Z., Kang, Q., Tao, W.-Q., Qiao, R., 2019. Predicting effective diffusivity of porous media from images by deep learning. Sci. Rep. 9 (1), 20387.
- Xu, T., Sonnenthal, E., Spycher, N., Pruess, K., 2004. TOUGHREACT User's Guide: A Simulation Program for Non-isothermal Multiphase Reactive Geochemical Transport in Variable Saturated Geologic Media. Lawrence Berkeley National Lab.(LBNL), Berkeley, CA (United States).
- You, J., Lee, K.J., 2021a. Analyzing the dynamics of mineral dissolution during acid fracturing by pore-scale modeling of acid-rock interaction. SPE J. 26 (2), 639–652.
- You, J., Lee, K.J., 2021b. Pore-scale study to analyze the impacts of porous media heterogeneity on mineral dissolution and acid transport using Darcy–Brinkmann–Stokes method. Transport Porous Media 137 (3), 575–602.
- You, J., Lee, K.J., 2021c. A pore-scale investigation of surface roughness on the evolution of natural fractures during acid dissolution using DBS method. J. Petrol. Sci. Eng. 204 108728
- Zaheer, M., Reddi, S., Sachan, D., Kale, S., Kumar, S., 2018. Adaptive methods for nonconvex optimization. Adv. Neural Inf. Process. Syst. 31.
- Zhang, A., Lipton, Z.C., Li, M., Smola, A.J., 2021. Dive into deep learning. arXiv preprint arXiv:2106.11342.